Supporting Information for

Exploring Metabolic Aberrations After Intracerebral Hemorrhage In Vivo with Deuterium Metabolic Spectroscopy Imaging

Xinjie Liu[1,2], Qingjia Bao[1,2*], Zhuang Liu[1,2], Jie Wang[1,2], Martins Otikovs[3], Zhi Zhang[1,2], Xin Cheng[1,2], Jiazheng Wang[5], Lucio Frydman[3], Xin Zhou[1,2,4], Maili Liu[1,2,4], Chaoyang Liu[1,2,4*]

[1] State Key Laboratory of Magnetic Resonance and Atomic and Molecular Physics, Innovation Academy for Precision Measurement Science and Technology, Chinese Academy of Sciences, Wuhan 430071, China

[2] University of Chinese Academy of Sciences, Beijing 100864, China

[3] Weizmann Institute of Science, Department of Chemical and Biological Physics, 234 Herzl Street, Rehovot, 76100, Israel

[4] Optics Valley Laboratory, Hubei 430074, China

[5] Clinical & Technical Support, Philips Healthcare, Beijing 100000, China

*Corresponding authors: Qingjia Bao, Email: qingjia.bao@apm.ac.cn;

Chaoyang Liu, Email: chyliu@apm.ac.cn;

S

Section 1. ^{1}H-^{2}H double-resonance coil with ^{2}H channel active detuning

To achieve both anatomical and metabolic imaging with ^{2}H magnetic resonance imaging, we designed a ^{1}H-^{2}H dual-resonance radiofrequency (RF) coil that uses proton signals as anatomical references for high-resolution images and obtains metabolic information from ^{2}H signals. The dual resonance coil design scheme solves the problem of inaccurate positioning caused by coil replacement during magnetic resonance imaging (MRI) experiments, which enhances the accuracy of MRI image registration. Additionally, the ^{2}H coils adopt a separate receiver and transmitter coil design scheme, which increases the B_1 homogeneity and the signal acquisition sensitivity. The proposed coil comprises five parts: RF shielding, ^{1}H transceiver birdcage coil, ^{2}H transmitting saddle coil, ^{2}H receiving double-loop surface coil, and ^{2}H active detuning circuit.

RF shielding layer

The RF shielding layer encloses the RF coil, creating electromagnetic isolation and reducing the coupling from gradient coils, shim coils, and magnets. To avoid eddy currents caused by the fast switch of the gradient, we adopted copper bars connected to the non-magnetic capacitor, rather than the whole copper structure, as shown in Fig. S1A. This design of RF shielding can reduce the coupling from gradient coils and enhance the uniformity and stability of the RF coils without introducing eddy current. There are 13 copper bars around the coil, each 200 mm long, 20 mm wide, and 0.1 mm thick, with a gap width of 4 mm. Figs. S1B and C show the simulation of the magnetic field with and without a shielding layer. A non-magnetic capacitor with a capacitance of 3.3 nF is welded between each gap, which maintains the electrical continuity of the shielding layer to prevent the RF field (300 MHz) from entering the gradient and uniform coils.

After the addition of the shielding layer, the current of the coil inside the RF shielding layer generates a reverse current outside the RF shielding layer. This reverse mirror current generates a magnetic field opposite to the original current, which weakens the original magnetic field. To analyze the effect, multiple sets of magnetic field simulations were conducted by setting shielding

layers of different diameters outside a fixed-size birdcage coil of 72 mm (refer to Table S1). The center's field strength increases gradually with the diameter of the shielding layer. However, to account for the magnet aperture and probe diameter, the diameter of the shielding layer is set to 100 mm (refer to Fig. S1C).
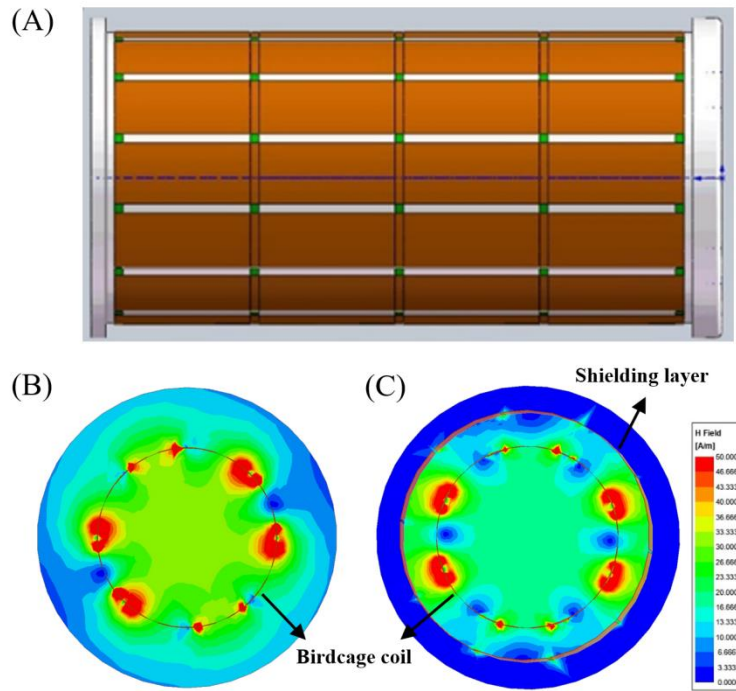
Figure S1. (A) The structure design of the shielding layer. (B) Magnetic field simulation without the shielding layer. (C) Magnetic field simulation with the shielding layer diameter size of 100 mm.

Table S1. Simulation of field strength with different shielding layer diameter

Diameter (mm)	Radiofrequency field strength (A/m)
90	12.43
95	14.29
100	18.54
105	20.61
110	22.88

¹H transceiver birdcage coil

We designed a ¹H transceiver coil with a birdcage structure to detect ¹H magnetic resonance signals. Considering the size of magnet aperture and shielding layer, the diameter and length of the birdcage coil were set to 72 mm and 70 mm, respectively. The structure is shown in Fig. S2A. Through physical debugging of the birdcage coil, non-magnetic capacitors of 8.9 pF were soldered onto the end ring, and two adjustable capacitors with an range of 1–4 pF were soldered at the symmetrical position of the end ring, which tune and match the coil around the working resonant frequency (tuning range is 296.5–303.5 MHz).

We conducted both electrical performance and MRI experiments. We also compared the MRI with the Bruker Volum coil (Bruker, Billerica, MA). Fig. S2B shows the ¹H coil S11, and the calculated Q value of the coil is 71.78. We acquired ¹H images using fast low-angle shot (FLASH) and rapid acquisition with refocused echoes (RARE) sequences for signal-to-noise ratio (SNR) calculations with the following parameters: field of view (FOV), $20{\times}20$ mm^2; matrix, $256{\times}256$; repetition time/echo time (TR/TE), 2000/48 ms for RARE, 200/4 for FLASH; slice thickness, 2 mm; number of acquisitions, 2; number of repetitions, 2. Fig. S2C shows the imaging results, which indicated that the image SNR for our coil is low compared with the Bruker coil (FLASH: ours 24.1, Bruker 32.9; RARE: ours 43.3, Bruker 46.5). The main reason is that the Bruker coil is a dual-channel orthogonal coil, while ours is a single coil. However, it is sufficient for acquiring ¹H anatomical images and shimming the magnetic field.
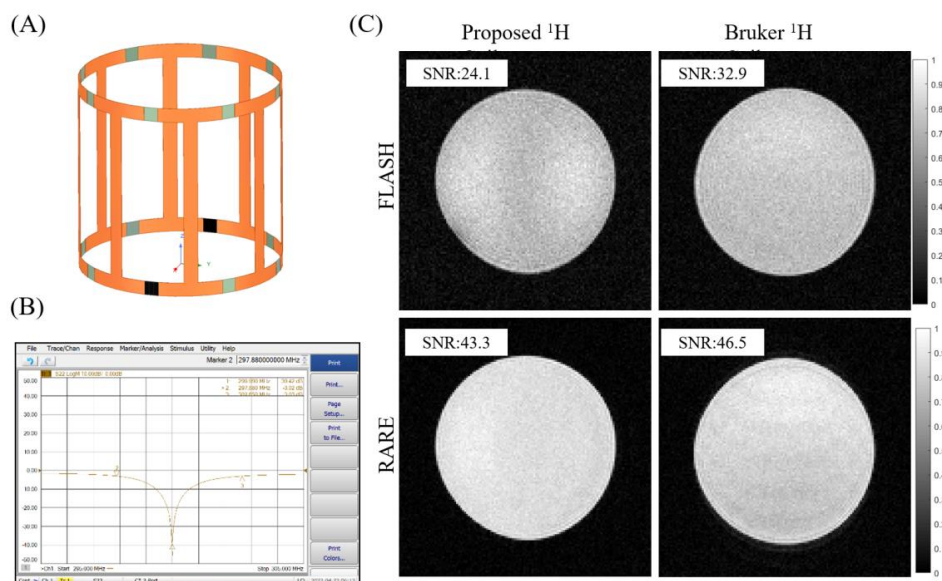
Figure S2. (A) The design of the ^1H birdcage coil. (B) Electrical parameters S11 of the ^1H coil. (C) Magnetic resonance images acquired by proposed coil and Bruker coil with fast low-angle shot (FLASH) and rapid acquisition with refocused echoes (RARE) sequences.

^2H transmitting saddle coil

We adopted a saddle-coil design for ^2H transmission to reduce the shield effect for the ^1H coil. To obtain the most homogenous B_1 field for ^2H excitation, we also optimized the coil length-to-diameter ratio. The simulation results showed that the most homogenous B_1 field is obtained when this ratio is set to 1.661. Considering the dimensions of the outer coil and the innermost double-loop coil, the diameter and length of the saddle coil were set to 48 mm and 80 mm, respectively. The structure of the ^2H transmission coil is shown in Fig. 3A and the B_1 field map is shown in Fig. 3B.

Moreover, to reduce coupling with the ^1H coil, the central plane of the saddle-coil opening angle coincided with the RF field of the birdcage coil. At this time, the RF field directions of the two coils are perpendicular to each other, as shown in Fig. S3C and D. Through debugging of the birdcage coil, a series of non-magnetic capacitors with 50 pF and 82 pF were welded at the 60° opening angle of the saddle coil and two adjustable capacitors with a range of 1–20 pF were welded at the feeding position, which tune and match the coil around the working resonant frequency (tuning range is 44.6–48.2 MHz) and enhance the pressure-bearing capacity of the non-magnetic capacitor to prevent it from breaking down.
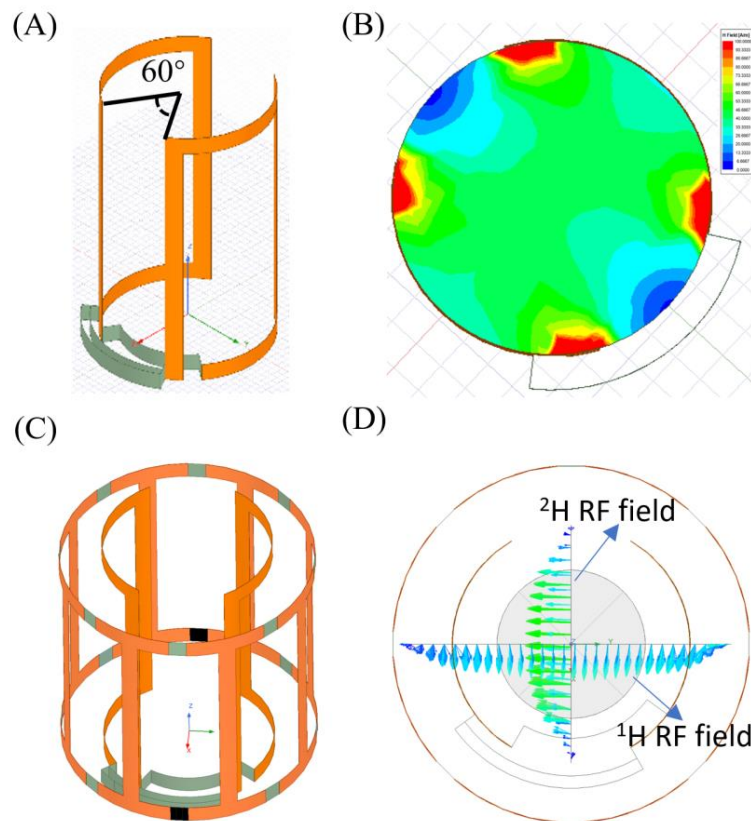
Figure S3. (A) The design of the ^{2}H saddle coil with an opening angle of 60°. (B) Magnetic field distribution for the ^{2}H saddle coil. (C) The arrangement of the ^{1}H birdcage coil and ^{2}H saddle coil. (D) Radiofrequency field simulation showed that the directions of the two coils are perpendicular to each other.

^{2}H receiving double-loop coil

Considering the FOV and the SNR, we set the size of the ^{2}H surface reciever coil to 18×18mm. To enhance the strength and uniformity of the B_1 magnetic field of the ^{2}H coil area, a dual-loop surface coil structure with overlapping appropriate areas was proposed, as described in Fig. S4B. In addition, a transceiver single-loop surface coil was made for comparison (Fig. S4A). The magnetic field simulation results (Fig. S4C, D) showed that the double-loop structure had stronger magnetic field strength and better uniformity than the single-loop structure. To make the surface coil resonate at the target frequency (46 MHz), a non-magnetic capacitor of 306 pF is welded, and two adjustable capacitors with a range of 1–20 pF were welded at the feeding position for tuning and matching the coil (tuning range is 44.7–47.5 MHz).
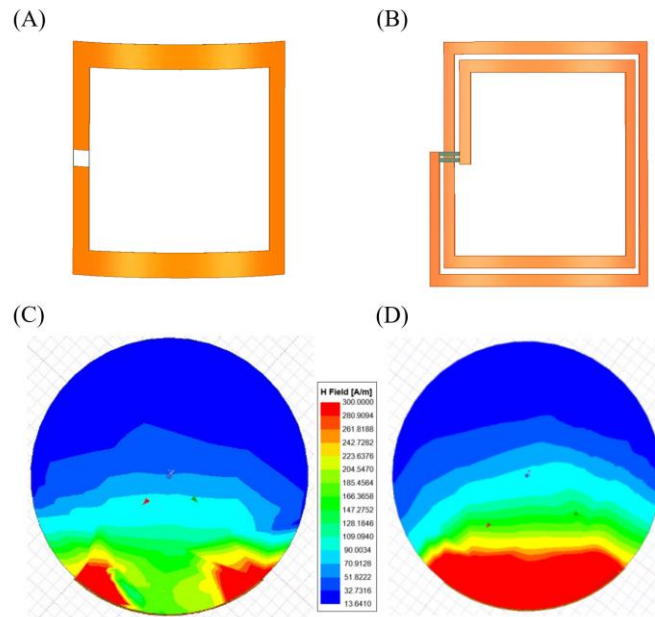
Figure S4. The ^{2}H surface coil structure design of single-loop (A) and double-loop coils (B). The simulated B$_1$ field for single-loop (C) and double-loop coil (D) showed that the double-loop structure had stronger magnetic field strength and better uniformity.

The improvement in SNR offered by the dual-loop receiver coil was evaluated using a phantom experiment, as illustrated in Figure S5. It is evident that the images obtained with a dual-loop receiver (third column) exhibit a higher SNR than those obtained with a single-loop receiver (second column) when using the same saddle excitation coil. Secondly, a saddle volume coil was utilized for excitation, thereby enhancing the uniformity of the excitation B$_1$ field. The images obtained with the saddle excitation coil (the second column) are more homogeneous than those obtained with the transceiver surface coil (the first column).

Additionally, the adiabatic pulses were applied to the surface coil to ascertain the SNR gain achieved by the saddle coil. The adiabatic pulse was a sech pulse with a duration of 1 ms and a bandwidth of 20250 Hz. The results are presented in Fig. S6. It is evident that the adiabatic pulse can enhance the SNR in comparison to the SLR pulse. Furthermore, the use of a volume coil for excitation has been demonstrated to yield superior image quality compared to that achieved with a surface coil and an adiabatic pulse excitation. The one-dimensional profile obtained from the center of the image also demonstrates the enhancement in SNR achieved by our new coil.
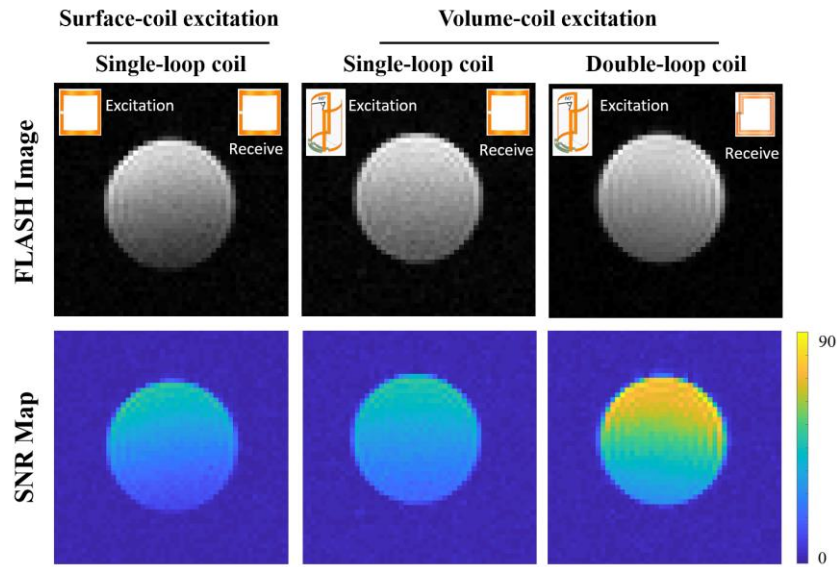
Figure S5. The ^{2}H FLASH images and the SNR maps calculated from FLASH images. The first column is the ^{2}H images with single-loop surface coil excitation and receiver, and the second column is from volume saddle excitation coil and single-loop surface coil for the receiver. The last column is from the volume saddle excitation coil and dual-loop surface coil for the receiver.
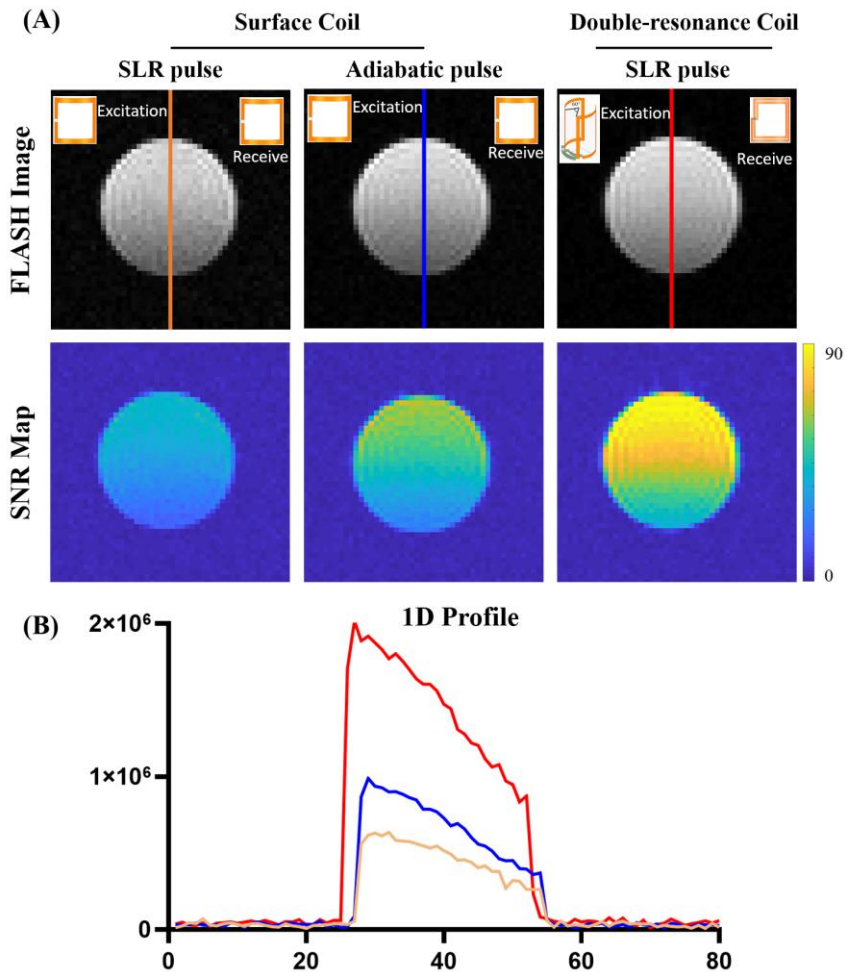
Figure S6. (A) The ^{2}H FLASH images and the SNR maps calculated from FLASH images. The first column is the ^{2}H images obtained by the transceiver single-loop surface coil with SLR pulse excitation; the second column is from the transceiver single-loop coil with adiabatic pulse excitation; the last column is from volume saddle coil with SLR pulse excitation and dual-loop surface coil for receiver. (B) The 1D profiles are taken from the center of the FLASH image.

^{2}H active detuning circuit for separating transmitting and receiving

Because the ^{2}H saddle and surface coils have the same resonance frequency, there will be strong coupling between these two coils if they operate simultaneously, which will impair the performance of the coils and may damage the preamplifier and power amplifier. To avoid this, we designed the active detuning circuits to ensure that the saddle and surface coils work in a time-sharing mode; the detailed detuning circuits are shown in Fig. S7A. The saddle coil adopts reverse active detuning (Fig. 7A, blue box). C2 is the resonant capacitance of the coil. We inserted the PIN diode into the resonant circuit of the saddle coil, and used direct current (DC) bias to control the PIN diode, thereby achieving resonance detuning of the saddle coil. C1 is the DC isolation capacitor on the feeding chain to prevent DC current from entering the power amplifier. L2 and L3 are choke inductors to prevent RF signals from entering the DC circuit in series. The ^{2}H receiving surface coil adopts active detuning (Fig. 7A, red box). The resonant capacitance of the coil consists of C1 and C2 connected in series in the figure. In the transmission stage, the DC bias circuit turns on a PIN diode, and C2, C5, and L3 form a trap-blocking circuit. By adjusting the value of L3, it resonates in parallel at a frequency of 46 MHz to present a high resistance state, and the receiving coil is detuned. During the receiving phase, the PIN diode turns off and the coil operates normally in resonance. C4 in the figure is the DC isolation capacitor, and L2 is the choke inductance.

The working state of the two ^{2}H coils is controlled by a tuning/detuning switch, which is controlled by the BLANK unit of the transmit/receive system. As shown in the timeline of Fig. S7B, when the BLANK is at a voltage of 5 V, the saddle coil resonates to transmit the signal, and the

surface coil is detuned. Similarly, when the BLANK is at a voltage of 0 V, the saddle coil is detuned, and the surface coil resonates to receive the signal. The S11 parameter test results under the resonance and detuning states of the ^{2}H transmitting coil and receiving coil are shown in Fig. S7B. The resonance peak of the transmitting coil disappears when the receiving coil works, and the resonance peak of the receiving coil disappears when the transmitting coil works, which indicates that the active detuning circuit designed in this article works normally and can achieve time-sharing operation of the transmitting and receiving separation coils. In addition, we have designed a protection circuit to prevent the high-power RF signal emitted by the saddle coil from being inductively received by the surface coil during the transmission phase and to protect the preamplifier.

(A)
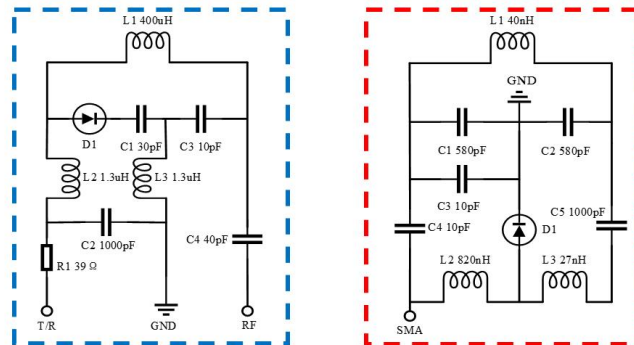
(B)
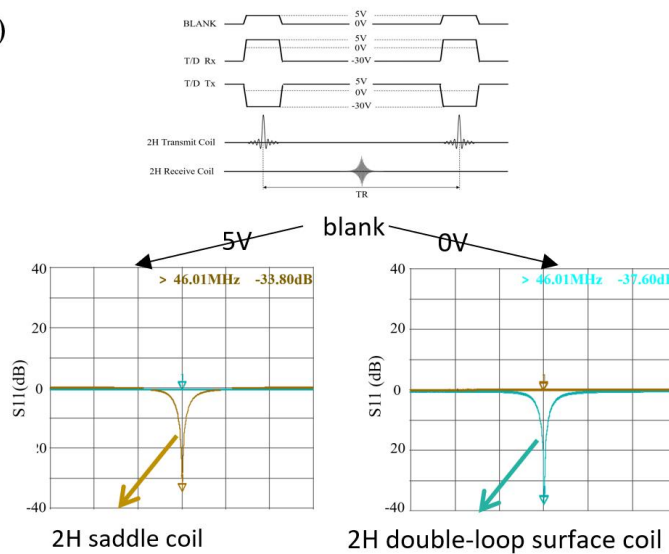
Figure S7. (A) The reverse active detuning circuits for the transmitting coil and active detuning

circuits for the receiving coil. (B) The working state of the two ^{2}H coils and the S11 parameter test results under the resonance and detuning states of the two coils.

Section 2. Optimization of the CSI-bSSFP sequence

Compared to conventional methods, balanced steady-state free precession (bSSFP) technology can achieve a high SNR per unit of time, making it an attractive choice for chemical shift imaging (CSI), especially for the metabolites with a high T_2/T_1 ratio. For the conventional CSI sequence based on FLASH technology, the signal intensity (SI) can be represented as: [1]

$$SI = M_0 \frac{(1 - E_1) \sin \alpha}{(1 - \cos \alpha \, E_1)} \tag{1}$$

where M_0 is the spin density, α is the flip angle, and $E_{1,2}$ is given by $e^{-TR/T1,2}$. Conventional CSI signal intensities depend on T_1, TR and flip angle α.

The CSI-bSSFP sequence is the application of bSSFP technology to CSI. bSSFP makes the longitudinal magnetization vector and transverse magnetization vector remain stable during the acquisition process. the signal intensity can be represented as: [2, 3]

$$SI = M_0 \frac{(1 - E_1) \sin \alpha}{1 - (E_1 - E_2) \cos \alpha - E_1 E_2} \tag{2}$$

From equation (2), the SI of the CSI-bSSFP sequence is determined by the TR, flip angle, and T_1 and T_2 values. It can be shown that, for given T_1 and T_2, the highest signal can be achieved at the flip angle α_{opt} given by: [3]

$$\alpha_{opt} = cos^{-1}\left(\frac{E_1 - E_2}{1 - E_1 E_2}\right) \tag{3}$$

The highest conventional CSI signal can be achieved at the flip angle α_{opt} given by:[1]

$$\alpha_{opt} = cos^{-1}(E_1) \tag{4}$$

Therefore, we also performed the signal simulation for different combinations of T_1 and T_2, as shown in Fig. S8. the simulation parameters were ae follows: TR, 20 ms; T_1 of water, 320 ms; T_1 of glucose, 64 ms; T_1 of Glx, 146 ms, and T_1 of lactate, 297 ms, and α optimized. For more combinations of T_2/T_1, the optimal CSI-bSSFP signal is around 10–50% of M_0 and still significantly higher than for conventional CSI signal.
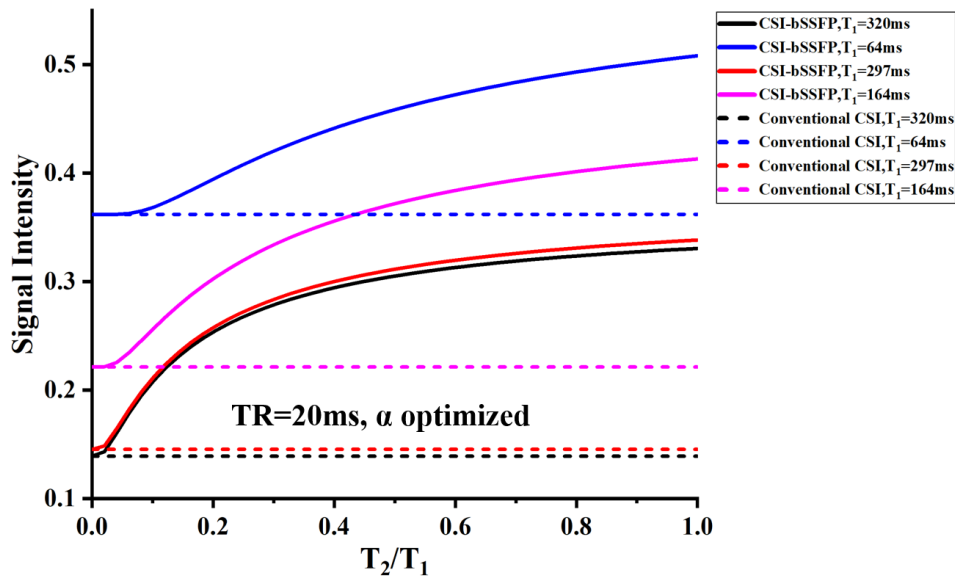
Figure S8. Steady-state signal for conventional CSI and CSI-bSSFP (TR=20 ms) for different combinations of T_1 and T_2 using optimized flip angles.

Section 3. Surgery and immunohistochemical analysis on rats

Construction of the intracerebral hemorrhage model

To establish the intracerebral hemorrhage (ICH) model in rats, we used the traditional methodology of collagenase injection into the caudate putamen nucleus (Cpu), comprising several meticulously executed steps. Initially, rats were administered an intraperitoneal anesthesia with 6% chloral hydrate, dosed at 0.6 mL per 100 g of bodyweight. Following sterilization, the anesthetized subjects were affixed within a stereotaxic device (RWD Life Science, Shenzhen, China), and a precise sagittal incision, measuring between 1.2 and 1.5 cm, was performed along the midline situated between the ears to fully expose the skull's anterior fontanel. Subsequently, a minuscule orifice of approximately 1.0 mm in diameter was drilled into the skull, with any resultant blood leakage meticulously cleansed using a cotton swab. The collagenase VII (Sigma-Aldrich, St. Louis, MO) saline solution, precisely measured at 2 μL with a concentration of 0.2 U/μL, was then administered into the Cpu, situated 5.5 mm beneath the skull's surface, over a span of 5 min (Fig. S9). The procedure necessitated the probe's retention at the injection site for an additional 10 min

post-injection before its careful extraction. The incision was sutured closed and disinfected with iodophor. Throughout the surgical procedure, meticulous attention was devoted to maintaining the body temperature of the rats within 25–28°C until they recovered.
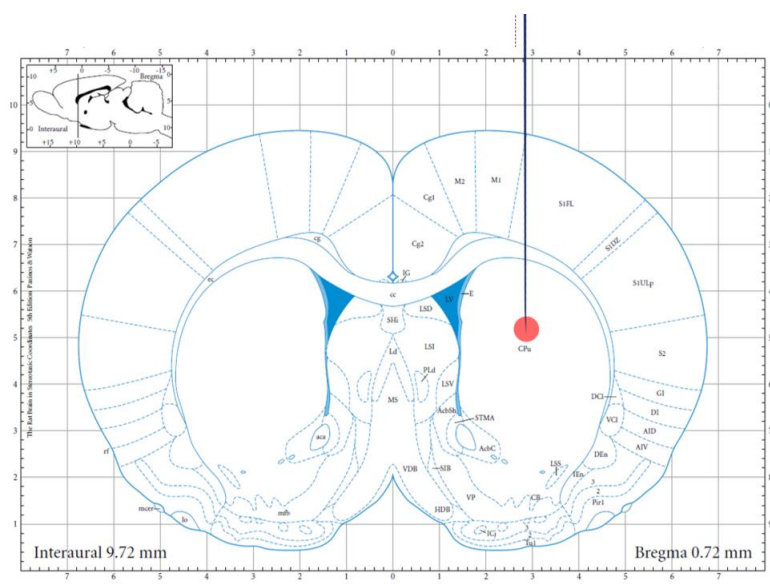
Figure S9. The intracerebral collagenase injection into the caudate putamen nucleus (Cpu) of rat brain to introduce construct the ICH animal model.

Immunohistochemical analysis

In a related series of procedures, three rat cohorts underwent scanning via ^{2}H-MRI/MRSI on predetermined dates. After that, they were subjected to anesthesia using 6% chloral hydrate at a dosage of 0.6 mL per 100g of bodyweight. This was followed by perfusion and fixation using 500 mL of precooled (4°C) normal saline and an equal volume of 4% paraformaldehyde fixative. Brain tissues were then thoroughly harvested and subjected to post-fixation in a 4% paraformaldehyde solution. The subsequent steps involved the embedding of the fixed brain specimens in paraffin, from which sections of 4 μm thickness were prepared using a freezing microtome (Kryostat 1720, Leitz, Wetzler, Germany), thereby facilitating staining and immunohistochemical analyses. Hematoxylin and eosin (HE) staining was meticulously conducted through a series of steps involving the initial immersion of tissue slices in a clarifying agent, followed by a gradual rehydration process through successive ethanol dilutions and final rinsing in distilled water. The slices were stained with Harris hematoxylin solution, differentiated in 0.8% hydrochloric acid

alcohol, and dyed with lithium carbonate solution, with intervening rinsing steps to remove excess dye. Eosin staining was achieved without subsequent rinsing in water. The dehydration process involved treatments with 95% and absolute ethanol, followed by clarification in xylene and mounting in neutral balsam. Immunohistochemistry for lactate dehydrogenase A (LDHA) entailed antigen retrieval, application of a blocking solution to prevent non-specific antibody binding, overnight incubation with a primary antibody specific to LDHA, application of a secondary antibody conjugated to a detection system, and visualization using chromogenic substrates, culminating in the mounting of the sections for long-term preservation.

Section 4. ^{2}H/HOD natural abundance and metabolites concentration conversion theory

In this study, we performed the NMR experiment to calculate the natural abundance ^{2}H/HOD concentration of the local water for rats. First, we get the ^{2}H NMR spectra from the standard sample (99.9% D_2O from Cambridge). Then, we perform ^{2}H NMR experiments with 5 water samples from the laboratory for rats, one of the experimental spectra is shown in Fig. S10 A. Then, the natural abundance ^{2}H/HOD concentration of the local water is calculated by comparing the NMR signals:

$$NA = \frac{S_{HOD}}{S_{D2O}} \times 0.999 \times 55.56 \times 2 \times 100\% \tag{5}$$

where NA refers to the natural abundance ^{2}H/HOD concentration of the local water, S_{HOD} represents the ^{2}H spectral integral of the water sample, S_{D2O} represents the ^{2}H spectral integral of standard D_2O samples, 55.56 represents the water concentration[4], and 2 represents the number of deuterons per water molecule. And the calculated natural abundance ^{2}H/HOD concentration of the local water is 15.75 mM, shown in the Fig. S10B. The calculated ^{2}H/HOD concentration of rat brain is 12.60 mM using formula (6).

$$CON_{HOD} = NA \times 0.8 \tag{6}$$

where CON_{HOD} refers to the ^{2}H/HOD concentration of rat brain, 0.8 represents the water content in brain tissue[4], NA refers to the natural abundance ^{2}H/HOD concentration of the local water.

To translate the intensities into metabolic concentrations, we first need to set up the signal

model for different pulse sequences, which considered T_1 and T_2 of HOD, Glc, Glx, and lactate. The simulated signal intensity of metabolites using non-localized spectroscopy and conventional CSI was calculated using formula (1), while the intensity with CSI-bSSFP was determined using formula (2), as shown in Fig. S11. Then, the concentration of substrates and metabolites was calculated by comparing the ^{2}H NMR signals to ^{2}H/HOD signal:

$$CON_{metabolites} = \frac{S_{metabolites}/SI_{metabolites}}{S_{HOD}/SI_{HOD} \times n} \times CON_{HOD} \tag{7}$$

where $CON_{metabolites}$ refers to the concentrations of substrates and metabolites, $S_{metabolites}$, S_{HOD} represents the ^{2}H NMR signal of metabolites, $SI_{metabolites}$, SI_{HOD} represents the simulation signal intensity of metabolites and ^{2}H/HOD, n represents the average number of deuterons per molecule, and CON_{HOD} refers to the ^{2}H/HOD concentration of rat brain.
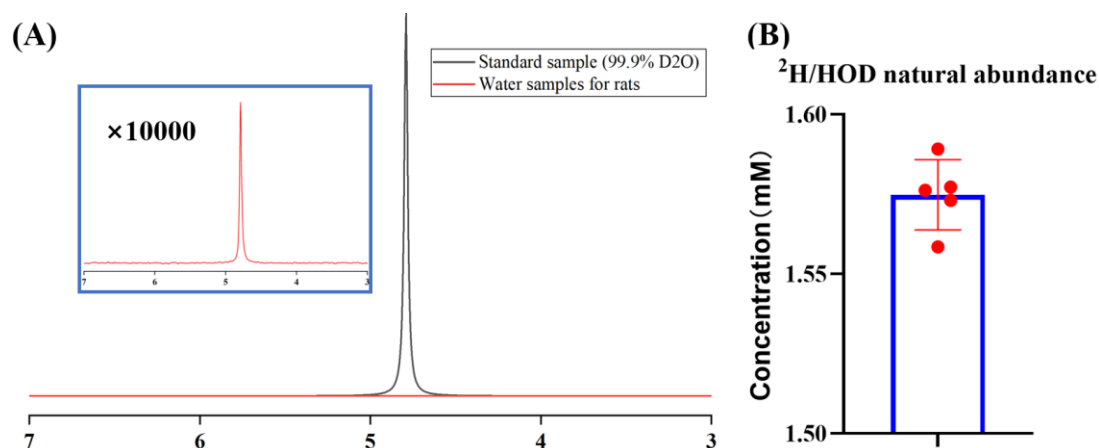
Figure S10. (A) The ^{2}H spectra of the standard sample and water sample from the laboratory for rats were obtained the ^{2}H NMR experiments. (B) The natural abundance ^{2}H/HOD concentration of the local water calculated by comparing the water sample signal to the standard sample signal.
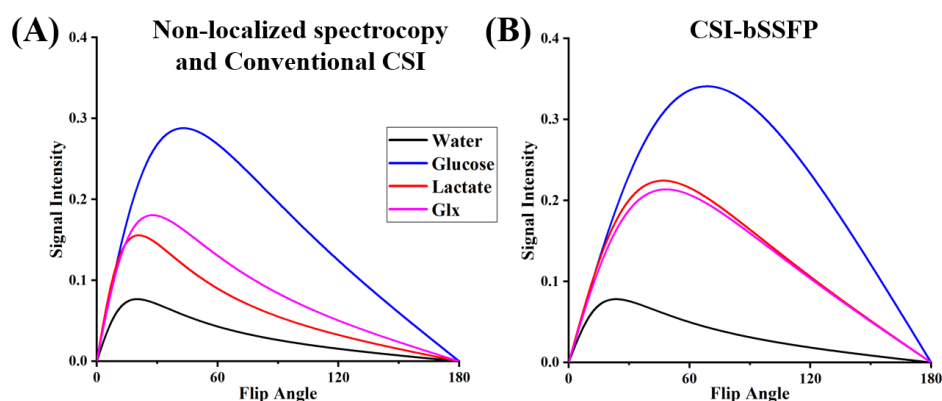
Figure S11. the simulation signal intensity of metabolites and water with different flip angles.

Section 5. the metabolic dynamic changes for glucose, glutamate/glutamine (Glx), and lactate

We performed the changes in various metabolites after injecting glucose, shown in Fig. S12. And the result is added to the Supporting Information.
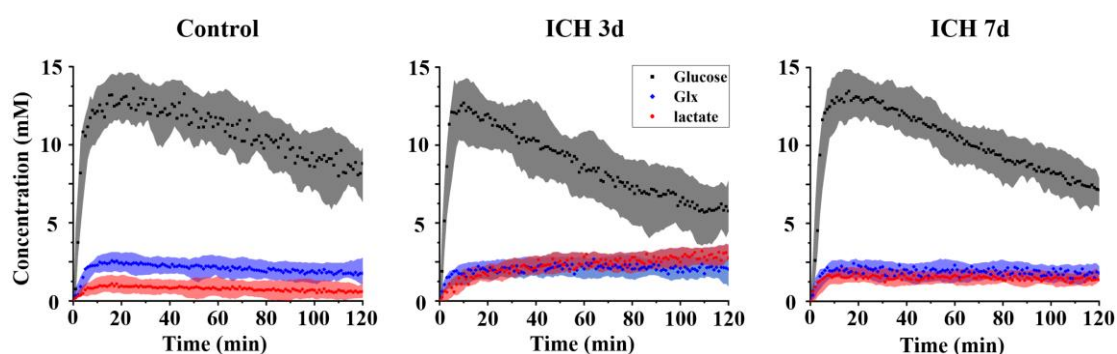
Figure S12. Dynamic concentration of glucose, Glx and lactate after [6,6'-^{2}H$_2$]-glucose injection. Each point in the figure shows the value at a specific timepoint for one animal, and the shaded area shows the data range of all animals in the group.

Reference

1.   Bernstein, M. A.; King, K. F.; Zhou, X. J., *Handbook of MRI pulse sequences*. Elsevier: 2004.
2.   Speck, O.; Scheffler, K.; Hennig, J., Fast 31P chemical shift imaging using SSFP methods. *Magn Reson Med* **2002,** *48* (4), 633-9.
3.   Bieri, O.; Scheffler, K., Fundamentals of balanced steady state free precession MRI. *Journal of Magnetic Resonance Imaging* **2013,** *38* (1), 2-11.
4.   De Feyter, H. M.; Behar, K. L.; Corbin, Z. A.; Fulbright, R. K.; Brown, P. B.; McIntyre, S.; Nixon, T. W.; Rothman, D. L.; de Graaf, R. A., Deuterium metabolic imaging (DMI) for MRI-based 3D mapping of metabolism in vivo. *Science advances* **2018,** *4* (8), eaat7314.